American Mineralogist, Volume 84, pages 1117–1125, 1999

Burbankite, a (Sr,REE,Na,Ca)-carbonate in fluid inclusions from carbonatite-derived fluids: Identification and characterization using Laser Raman spectroscopy, SEM-EDX, and synchrotron micro-XRF analysis

BERNHARD BÜHN,[1,2,*] ANDREW H. RANKIN,[2] MARTIN RADTKE,[3,4] MARTIN HALLER,[3] AND ARNDT KNÖCHEL[5]

[1]Institut für Geowissenschaften der Universität, Senckenbergstrasse 3, D-35390 Giessen, Germany
[2]School of Geological Sciences, CEESR, Kingston University, Penrhyn Road, Kingston-upon-Thames, Surrey KT1 2EE, U.K.
[3]HASYLAB/DESY, Notkestrasse 85, D-22603 Hamburg, Germany
[4]Laboratorio Nacional de Luz Sincrotron, Caixa Postal 6192, CEP 13083-970 Campinas SP, Brazil
[5]Institut für Anorganische und Angewandte Chemie der Universität, Martin-Luther-King-Platz 6, D-20146 Hamburg, Germany

ABSTRACT

Burbankite, ideally $(Na,Ca)_3(Sr,REE,Ba)_3(CO_3)_5$, is a rare REE carbonate mineral that until now had been encountered only at a few localities including highly alkaline silicate rocks, carbonatites, and lacustrine sediments. It was identified as an abundant solid phase in fluid inclusions that represent fluids derived from the Kalkfeld carbonatite complex (Namibia). Burbankite occurs in association with other solids including nahcolite, halite, sylvite, rouvilleite (?), fluorite, calcite, cryolite, base metal sulfides, and phosphates. The carbonatite-derived fluids were trapped in quartzite country rocks close to the carbonatite contact. The optical and geochemical identification of burbankite has been confirmed by confocal Laser Raman spectrometry. The burbankite crystals show a Raman shift at 1078 cm^{-1}, which is significantly displaced relative to peaks for other common carbonates and is much broader. The elemental composition of burbankite was determined by a combination of SEM-EDX on opened inclusions and synchrotron-XRF analysis on unopened wafers. The SEM-EDX analyses of the burbankite crystals yielded a compositional range (in wt%) of Na_2O 10.6–17.5, CaO 3.6–17.4, SrO 12.0–26.7, BaO 2.5–5.5, La_2O_3 3.5–7.0, Ce_2O_3 4.7–9.0, Nd_2O_3 0.9–2.1, and CO_2 (calc.) 29.8–35.2. The Na/Ca ratios are between 1.0 and 4.3, which is high in comparison with rock-forming burbankite occurrences, and clearly distinguishes the burbankite crystals from carbocernaite. Synchrotron micro-XRF spectra yielded REE patterns decreasing from La to Yb over 2.5 orders of magnitude with small negative Eu anomaly $[(Eu/Eu^*)_{cn} = 0.5–1.0]$ in some cases. The Y/Ho ratios range from 1 to 5, and Th/U ratios are between 1 and 10. The fluids trapped are interpreted to represent a highly evolved but pristine, alkali-rich, hydrous, carbonate melt, which had not lost alkalis to the country rocks by fenitization processes. The common occurrence of burbankite crystals in the fluid inclusions shows the high capability of carbonate melts and fluids to transport high-field-strength and large-ion-lithophile elements.

INTRODUCTION

Carbonatite melts derived from a partially molten metasomatized mantle source have a high potential to transport alkalis, large-ion-lithophile and high-field-strength elements. Their relatively high overall content of fluid and gaseous components such as CO_2, H_2O, and halogens means that they have low viscosities (e.g., Wolff 1994), and are able to flow very readily at moderate to low temperatures. Carbonatite melts, therefore, behave like highly mobile fluids, and have the ability to penetrate and mineralize crustal rocks to form economically important ores of REE, Sr, Th, U, F, or Fe, among others. Crystallized carbonatite melts, however, generally have lost their alkali and volatile components to associated metasomatic fluids. Therefore, whole-rock analyses of carbonatite rocks may not be representative of the compositions of the initial carbonatite magma. Only when both alkali-rich fluids and carbonatite melts are trapped (e.g., in fluid inclusions), do they together represent the pristine carbonatite melt compositions.

We report here on the identification and comprehensive geochemical characterization of the mineral burbankite, ideally $(Na,Ca)_3(Sr,REE,Ba)_3(CO_3)_5$, which occurs as a solid phase in multicomponent carbonatite-derived fluid inclusions. The investigated fluids were trapped in quartzites in the immediate vicinity of the Kalkfeld carbonatite complex (Namibia) and are interpreted to represent a carbonatite melt with all volatile components preserved. Burbankite is a rare mineral confined mainly to highly alkaline igneous rocks (e.g., Verwoerd 1963; Chen and Chao 1974), but it also has been reported from the alkaline lacustrine environment of the Eocene Green River Formation, U.S.A. (Milton and Fahey 1960; Fitzpatrick and

*E-mail: Bernhard.Buehn@geo.uni-giessen.de

Pabst 1977). Recently, burbankite has been described in carbonatite from the Khibina complex in Russia (Zaitsev et al. 1998). To the best of our knowledge, however, it has not been identified previously in fluid inclusions.

In contrast to the analysis of the fluid species in inclusions (Vanko et al. 1993; Mavrogenes et al. 1995; Philippot et al. 1998), the quantitative analysis of solid phases in fluid inclusions—with the approach applied here—allows the use of internal reference elements for concentration determinations. The significance of identifying solid phases in fluid inclusions is that they contain elements that were previously present in solution at higher temperatures, and therefore provide us with the means to estimate fluid compositions at the temperature of entrapment. In the case of burbankite, its identification and high volumetric proportion in fluid inclusions demonstrates the ability of evolved carbonatite melts/fluids to carry large amounts of REE and Sr.

A variety of optical, crystallographic, X-ray, and spectroscopic methods have been used to identify solids in fluid inclusions (Roedder 1990) including those associated with carbonatites (Rankin and Le Bas 1974; Metzger et al. 1977; Ting et al. 1994; Xie et al. 1996). Previous attempts to determine the major, minor, and trace element composition of such crystals have been hampered by their small size and general inaccessibility, which does not allow the use of analytical techniques applied to polished surfaces. We apply here confocal Laser Raman spectroscopy for the identification of burbankite, and a combination of SEM-EDX and synchrotron-XRF (SXRF) techniques for a comprehensive geochemical characterization. With the recent development of SXRF microprobe methods, it is possible to achieve sufficient penetration depth and beam resolution for quantitative microanalysis. The primary objectives of this study were to identify burbankite and determine its major and trace element composition as a mineral phase crystallized from a pristine, volatile-rich carbonatite melt. Secondly, the approach shows that the complementary nature of SXRF and SEM-EDX methods provides a powerful means for determining, quantitatively and semi-quantitatively, a broad geochemical spectrum of elements present in burbankite crystals down to the parts per million level.

SAMPLE DESCRIPTION

The samples studied are from country rocks surrounding the Cretaceous Kalkfeld carbonatite complex in north-central Namibia, which is intruded into Pan-African granites and metasediments (Prins 1981). The country rocks show abundant metasomatism (fenitization) related to the carbonatite in the form of feldspathization and growth of aegirine-augite, chlorite, and iron-oxides. In the vicinity of the contact, the quartzites and granitic country rocks contain abundant multi-phase fluid inclusions in quartz, consisting of solid, aqueous, and carbonic components in variable proportions. This fluid inclusion population is restricted to country rocks close to the contact, and quartzites away from the carbonatite complex only contain a low abundance of two-phase, low-salinity aqueous inclusions. The fluid inclusions studied here, therefore, are interpreted to represent fluids derived from the Kalkfeld carbonatite complex.

Based on optical, Raman spectroscopic, SEM-EDX, and synchrotron-XRF methods, we have identified several solids in the fluid inclusions including nahcolite, halite, sylvite, a (Na,Ca,Mn,Fe)-fluorocarbonate [probably rouvilleite $Na_3(Ca,Mn,Fe)(CO_3)_3F$], fluorite, (Mn,Fe)-bearing calcite, cryolite, various Fe-Cu-Zn-As sulfides, a few phosphates, and a REE-bearing mineral that we show belongs to the burbankite group of REE-carbonates; small amounts of other unidentified crystals are also present. The burbankite crystals have a high birefringence and tend not to develop distinct crystal forms.

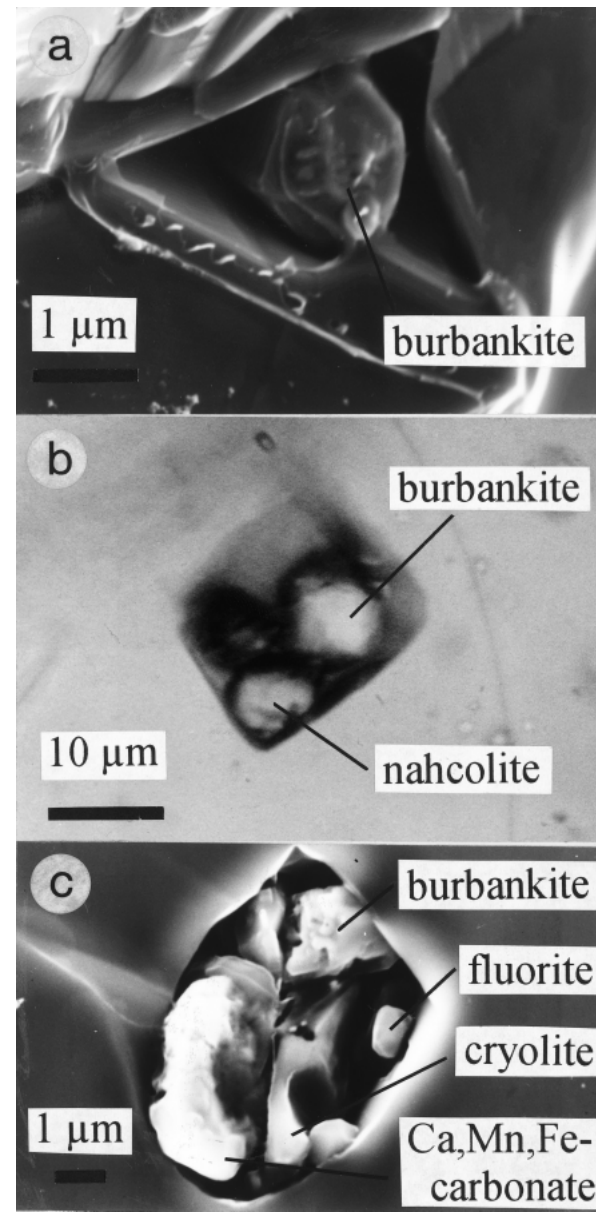

FIGURE 1. (a) SEM image of a single burbankite crystal in an inclusion pit. Note the hexagonal shape of the burbankite. **(b)** Optical photomicrograph of an aqueous fluid inclusion containing burbankite in association with nahcolite. **(c)** SEM image of burbankite coexisting with fluorite, (Ca,Mn,Fe)-carbonate, and cryolite in an inclusion pit.

They rarely exceed 10 μm in diameter. Many inclusions contain a high volumetric proportion of solid phases, which would classify them as melt inclusions or as fluid inclusions that have necked-down. In many inclusions, burbankite is a dominant phase and may occupy up to 50% of the inclusion volume. The inclusions mostly decrepitate upon heating to 300 ºC before dissolution of burbankite. Any combination of solids, aqueous liquid, and carbonic liquid/vapor can be observed in the inclusions. This is exemplified in Figure 1 showing burbankite as a single, hexagonal crystal in an inclusion pit (Fig. 1a), in association with nahcolite (Fig. 1b), and in assemblage with other solid phases (Fig. 1c). Thus, the burbankite crystals and all other solid phases are not daughter minerals sensu strictu. Rather, their highly variable volumetric proportions and assemblages suggest extremely inhomogeneous conditions of entrapment and/or necking-down processes, which was due probably to rapid quenching of the fluids when they were emplaced into the host quartzites.

Analytical techniques

Confocal Laser Raman spectroscopy was performed on a polished section of a burbankite reference material and on doubly polished quartz wafers of the sample material containing suspected burbankite. Analyses were carried out using a Dilor LabRam 1B system with a 1.8 mW He-Ne laser and also a Renishaw Raman 100 system with a 2.0 mW Ar laser. Both machines use a CCD detector. The counting time was 60 s. The spectra acquired with the two different machines are identical.

The SEM-EDX and SXRF analyses were performed on doubly polished wafers ~200 μm thick. Chemical analysis of the grains was carried out on both opened (SEM-EDX) and unopened (SXRF) inclusions. The rationale behind using these two methods was to quantify lighter elements (Na to Ba except for Y) via SEM-EDX, and heavier elements (Ba, REE, Y, Th, and U) with SXRF, with Ba serving as an internal standard element for synchrotron-XRF analysis as described below. Previous attempts to quantify the chemical composition of solid phases in opened fluid inclusions by SEM-EDX have recognized the pitfalls associated with this technique (e.g., Metzger et al. 1977). In more recent years, several publications have presented reliable data, which come close to a quantitative analysis in some cases (Anthony et al. 1984; Farrow et al. 1991; Molnar et al. 1997). Nevertheless, extreme care has to be taken for data acquisition, which means a careful selection of properly exposed crystals and further generous screening for reliable X-ray spectra to which a quantification procedure can be applied with confidence. For our study, we broke the wafers and mounted them on the sample holder with the freshly exposed surface upward, so that the crystals were exposed directly to the electron beam. Analyses were carried out with a JEOL JSM-6310 using an accelerating potential of 15 kV and a beam current of 0.75–1.5 nA, depending on the spot size of the electron beam. Energy-dispersive analyses were performed with an Oxford Instruments ISIS fitted with a Pentafet SATW detector. The counting time was 300 s lifetime to prevent evaporation, especially of Na. The small size of the crystals did not permit use of a defocussed electron beam. Natural standards were used for Na (jadeite), Ca (wollastonite), and Ba (barite), and synthetic minerals for Sr (SrF_2), La (LaB_6), Ce (CeO_2), and Nd (NdF_3). The quantification method used is based on a ZAF correction included in the software package supplied by Oxford Instruments. In principle, this procedure is designed for flat sample surfaces only, so that it is crucial to reduce the uncertainties derived from rough-surface analysis to a minimum. It is essential that the takeoff angle be 60° and that no neighboring grains interfere with the burbankite spectrum (see also Anthony et al. 1984). The samples were tilted individually for each analysis to obtain the flattest burbankite surface possible and to ensure that no host quartz or other mineral grains occur within the path of the X-ray emergent (takeoff) angle. However, some secondary fluorescence of Si was always present. The Na*K*, Ca*K*, Sr*L*, Ba*L*, and REE*L* fluorescence lines were measured. Only spectra that did not display a decrease in background counts at the low-energy end, and that, in this respect, compared favorably with the peak/background relationship of the flat-surface burbankite standard spectrum, were quantified. In spite of these precautions taken with respect to absorption, the Na data must be taken as semi-quantitative. The quantification of Sr accounts for the partial overlap of Sr*L*α with Si*K*α X-ray line. There are no peak overlaps for Ca*K*, Ba*L*, and LREE*L* lines. The EDX data for Pr are not presented due to low concentrations, but the analyses yield consistent results for Pr that plot midway between chondrite-normalized Ce and Nd.

Synchrotron-XRF microanalyses were performed at beamline L of the Hamburg Synchrotron Laboratory (HASYLAB) at the Deutsches Elektronen Synchrotron (DESY), Germany. The white spectrum of the DORIS accelerator was used as the excitation source. With a critical energy of 16.5 keV, fluorescent K-shell X-rays can be excited for elements up to Pb. By the use of elliptically shaped lead-glass capillary optics, a hard X-ray beam of about 3 μm in diameter was achieved at minimum distance (0.5 mm) between the capillary tip and the wafer surface. The spectral distribution of the source is not influenced by the capillary up to 60 keV, which means that the capillary transmission function is equal to 1 (Janssens et al. 1998). The REE, Ba, and Y were detected via K-shell excitation, and peak overlaps were avoided. For the actinides, Th*L* and U*L* lines were measured. The beamline setup and further details on the focussing method are given by Haller and Knöchel (1996).

Solitary inclusions were selected to prevent interaction of the incident beam and the generated X-rays with other inclusions. Moreover, only inclusions between 10–30 μm below the quartz wafer surface were analyzed in order to minimize absorption effects. Based on scans over the particular fluid inclusions at 2 μm steps, long-time measurements of 900 s lifetime were taken on the spots with the highest count rates for Sr, REE, and Ba. Peak area determinations were done with the computer code AXIL, which belongs to the QXAS package (IAEA, Vienna). The quantification via fundamental parameter analysis (Haller and Knöchel 1996; Vincze 1995) uses a burbankite density of 3.54 g/cm^3 (Effenberger et al. 1985) and a mean crystal thickness of 10 μm. The quantification program includes a correlation for absorption, but not for secondary fluorescence. Due to the use of a white beam, enhancement effects are negligible. Density and thickness of the crystals have only a very minor effect on the results of the quantification. The absorption of Ba and REE*K*α lines by a quartz matrix is negli-

gible (Fig. 2). The actinide $L\alpha$ lines are absorbed to a very minor extent at the maximum depth of the measured inclusions of 30 μm, and the Th/U ratio is not affected at all. The correction for absorption in the burbankite crystals themselves uses a C, O, Na, Ca, Sr, Ba burbankite matrix. Because of the small size of the crystals, absorption of X-rays by the crystals is very little. In general, the relatively light quartz matrix and the small thickness of the burbankite grains caused only minor absorption of the high-energy photons measured here. This was established by varying the parameters (burbankite density, burbankite thickness and matrix, and quartz thickness), which caused no significant change in the calculated element concentrations. For example, a very light matrix consisting only of C and O would change the calculated Y content only by 5% relative, which hardly alters the Y/Ho ratio.

RESULTS

Identification by Laser Raman spectroscopy

A polished sample of burbankite coexisting with calcite from the Khibina carbonatite complex (Kola Peninsula, Russia), provided by the Department of Mineralogy of the Natural History Museum (London), was used as reference material for the burbankite crystals. Figure 3 depicts Raman spectra of the reference material and the burbankite crystals. The burbankite reference displays a Raman peak at 1078 cm^{-1} as the only significant Raman shift. The peak is displaced relative to the main calcite peak at 1086 cm^{-1} (obtained by analyzing the coexisting calcite in the reference sample) toward lower wave numbers, and is significantly broader than the calcite peak. The burbankite grains from the fluid inclusions reproduce this broad peak at 1078 cm^{-1} with no other significant peaks derived from other solid phases.

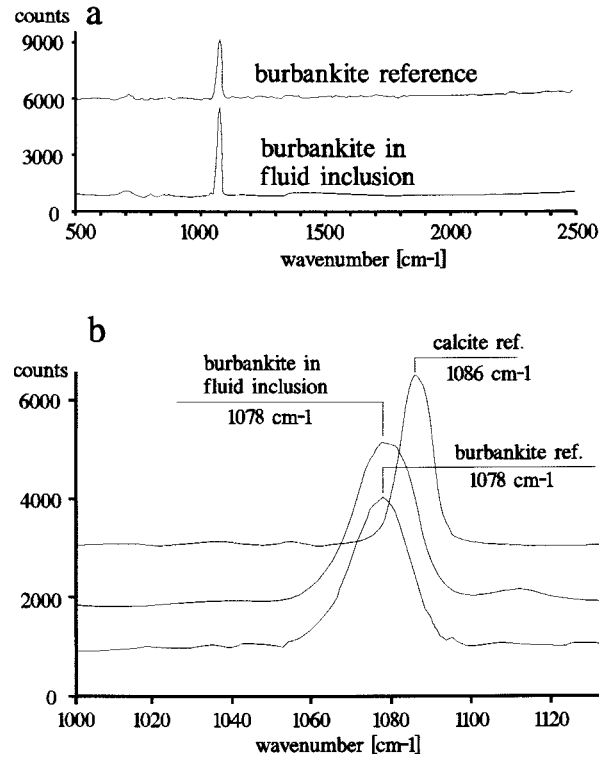

FIGURE 3. (a) Confocal Laser Raman spectra of the burbankite reference material and a burbankite crystal of the fluid inclusions. **(b)** Blow-up of the Raman spectrum showing the significant, broad burbankite peak at 1078 cm^{-1}, distinctly displaced from the narrow calcite peak at 1086 cm^{-1}.

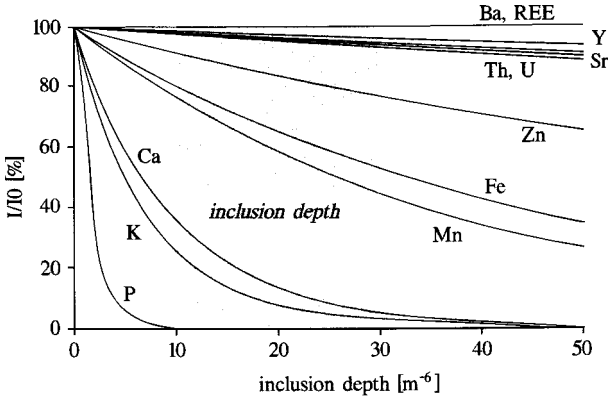

FIGURE 2. Absorption of $L\alpha$ (for Th and U) and $K\alpha$ lines (all other elements) of selected elements in a quartz matrix given in percent of I/I_0. At an inclusion depth between 10 and 30 μm used in this study, Ba and REE$K\alpha$ line absorption is virtually zero, while Y$K\alpha$, Th$L\alpha$, and U$L\alpha$ lines are absorbed to a minor extent.

Energy-dispersive X-ray analysis

Figure 4a shows an energy-dispersive spectrum of the burbankite standard with distinct peaks for Na, Ca, Sr, Ba, and LREE. The carbon peak partly derives from the carbon coating. This burbankite occurrence has been investigated comprehensively by Zaitsev et al. (1998) to which the reader is referred for details. The EDX spectrum of the reference material was quantified for comparison, yielding the composition given in Table 1 with Na/Ca (wt ratio)= 1.1, SrO = 18.1 (wt%), BaO = 4.2 (wt%), and ΣLa,Ce, and Nd (as oxides) = 16.5 wt%. This is in good agreement with wavelength-dispersive electron microprobe analyses (EMPA) of this burbankite occurrence provided by Zaitsev et al. (1998) (Table 1).

An EDX spectrum of the burbankite daughter crystals is shown in Figure 4b, displaying qualitatively the same peaks as the reference material. Table 1 lists four semi-quantitative analyses of the burbankite grains, which cover the range of chemical compositions of all burbankite analyses performed. The SrO content ranges between 12 and 27 wt%, ΣLREE (oxides except Pr_2O_3) between 9 and 17 wt%, and BaO between 2.5 and 5.5 wt%. The CO_2 content was calculated in the stoichiometric proportions of burbankite. The Na/Ca weight ratio varies between 1.0 and 4.3 but is mostly between 2 and 3 for all analyses performed.

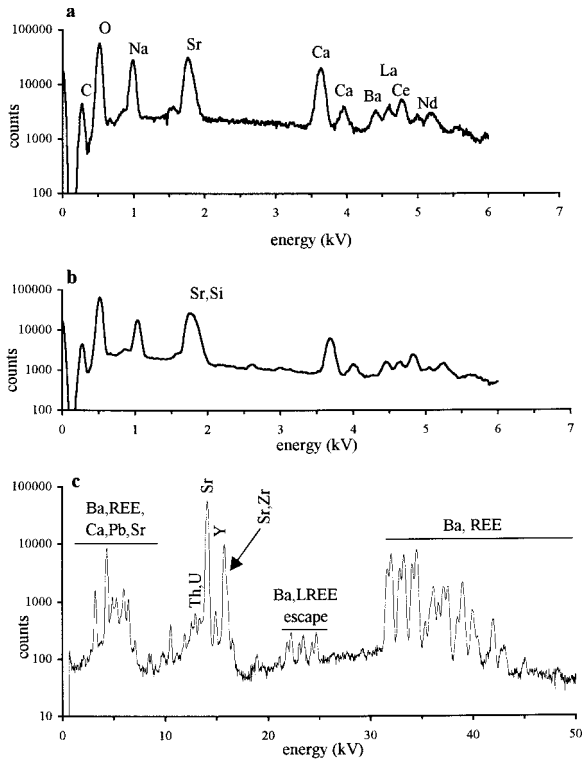

FIGURE 4. (a) Energy-dispersive spectrum (EDX) of the burbankite reference sample. **(b)** EDX spectrum of a burbankite crystal of the fluid inclusions. Note that Sr*L*α overlaps with Si*K*α from the host quartz. **(c)** Example of a synchrotron-XRF burbankite spectrum, analysis bb4975.

Burbankite is a hexagonal carbonate (compare Fig. 1a) with the ideal composition $(Na,Ca)_3(Sr,REE,Ba)_3(CO_3)_5$. Due to cation vacancies (Burt 1989; Miyawaki and Nakai 1996), burbankite may approach the chemical composition of orthorhombic carbocernaite with the ideal formula $(Ca,Na)(Sr,REE,Ba)(CO_3)_2$ (Effenberger et al. 1985; Burt 1989; Wall et al. 1993). Apart from the crystal structure, the main difference between burbankite and carbocernaite is the Na/Ca weight ratio and the cation/carbonate ratio (see Wall et al. 1993). Typically, Na/Ca ratios of carbocernaite are far below 1, being between 0.2 and 0.3 for carbocernaite from India (Table 1). The Na/Ca ratio can therefore be used to distinguish between burbankite and carbocernaite on chemical grounds (Zaitsev et al. 1998). Evaporation of Na by the electron beam or possible absorption effects on the Na*K* lines would have the effect of further lowering the Na/Ca ratio. Thus, the high Na/Ca ratio of one order of magnitude above that of carbocernaite clearly distinguishes the burbankite crystals from carbocernaite.

The sum of cations in the burbankite crystals falls within the range 5.9–6.6, scattering around the ideal value of 6.0. There is a distinct negative correlation between Ca and the LREE, not only in the burbankite crystal data set, but also when the literature data of rock-forming burbankite are included. For the four burbankite analyses presented here, Ca correlates with La at $R^2 > 0.9$; R^2 decreases down to 0.3 when all burbankite literature data are included. Although many other types of substitutions are possible in an Na,Ca-bearing carbonate with site vacancies (Miyawaki and Nakai 1996), the $LREE^{3+}$ seem to substitute essentially for Ca^{2+} in burbankite. There is a weak negative correlation between Ca and Ba for the entire burbankite

TABLE 1. (Semi-)quantitative EDX analyses of burbankite crystals compared to other burbankite, calcioburbankite, and carbocernaite occurrences in rocks

Sample	Burbankite crystals, Namibia				Burbankite reference	Burbankite reference	Burbankite Montana	Burbankite Montana	Burbankite Wyoming	Calcio-burbankite	Carbo-cernaite
Analysis	45	70	141	144	*	†	‡	§	||	#	**
Na_2O	17.0	10.6	17.5	13.1	11.8–12.6	12.9	10.17	8.34	10.47	15.17	3.8-4.8
CaO	17.4	3.6	4.3	5.5	10.1–12.6	12.1	13.68	11.47	8.00	11.81	15.9–17.8
SrO	12.0	25.6	25.7	26.7	17.7–24.7	18.1	19.70	25.08	15.61	7.65	18.7–24.0
BaO	2.5	5.5	3.0	5.2	0.8–6.7	4.2	14.02	11.47	5.73	0.46	1.0–1.7
La_2O_3	3.5	7.0	5.9	6.2	4.8–7.1	5.9	2.34	3.37	3.73	6.20	9.1–13.3
Ce_2O_3	4.7	9.0	8.0	8.8	7.0–11.1	8.7	4.65	5.39	8.65	14.38	8.7–10.3
Nd_2O_3	0.9	1.5	1.7	2.1	1.2–3.1	2.0	1.40	1.26	4.60	3.76	1.8–2.1
CO_2	35.2	29.8	33.9	33.3	33.4–34.8	34.3	33.39	33.24	29.73	35.13	31.8–32.8
Total	93.1	92.5	99.9	101.0		98.2	99.35	99.62	86.52	99.40	
Formula proportions of cations based on 15 oxygen atoms											
Na	3.44	2.54	3.68	2.79		2.66	2.17	1.78	2.38	3.07	
Ca	1.95	0.47	0.49	0.65		1.39	1.61	1.35	1.00	1.32	
Sr	0.72	1.82	1.61	1.70		1.12	1.26	1.60	1.06	0.45	
Ba	0.10	0.26	0.13	0.23		0.18	0.60	0.50	0.26	0.02	
La	0.13	0.32	0.24	0.25		0.23	0.10	0.14	0.16	0.36	
Ce	0.18	0.40	0.32	0.35		0.34	0.19	0.22	0.36	0.55	
Nd	0.03	0.07	0.06	0.08		0.08	0.06	0.05	0.19	0.14	
Total	6.55	5.88	6.53	6.05		6.00	5.99	5.64	5.41	5.98	
Na/Ca††	1.0	3.1	4.3	2.5	1.0–1.3	1.1	0.8	0.8	1.4	1.3	0.2–0.3

* Electron microprobe analysis, Khibina carbonatite (Zaitsev et al. 1998).
† Re-analyzed by SEM-EDX.
‡ In shonkinite rock (Pecora and Kerr 1953).
§ Re-analyzed by Effenberger et al. (1985).
|| In Green River Formation sediments (Fitzpatrick and Pabst 1977).
From Mont St. Hilaire, Ontario (Vanvelthuizen et al. 1995), totals including Pr and Sm.
** Carbonatite dike, India (Wall et al. 1993).
†† Weight ratio.

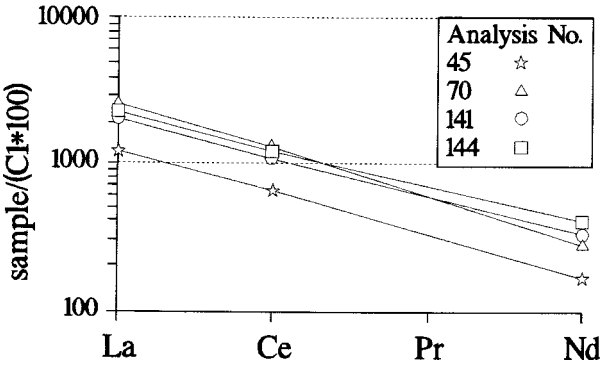

FIGURE 5. Chondrite-normalized LREE pattern of quantified EDX data from Table 1. Note the decrease from La to Nd of nearly one order of magnitude. C1 values from Anders and Grevesse (1989).

data set, but no distinct correlation of Ba with any other elements. It is not clear whether EDX peaks for F, as observed in some cases for the burbankite crystals in this study, are a bias from neighboring F-bearing mineral grains, or whether burbankite may also contain F as envisaged for carbocernaite by Harris (1972) and Speer (1990). Zaitsev et al. (1998) found only traces of F in their rock-forming burbankite, but the high F content of the trapped Kalkfeld fluids, as evidenced by the presence of fluorocarbonates, fluorite, and cryolite, suggests that the Kalkfeld burbankite crystals may be F-bearing. The REE La, Ce, and Nd can be quantified from the EDX analyses with confidence. All burbankite crystals, independent of their analytical totals, element composition, and Na/Ca ratios, display a very steep, straight LREE pattern with a decrease from La to Nd of nearly an order of magnitude (Fig. 5).

Synchrotron-XRF analysis

The high-resolution spot analyses show Sr, REE, and Ba as the main elements in the SXRF spectra of the burbankite crystals (Fig. 4c). Further peaks of interest are for Y*K*α, Th*L*α, and U*L*α. Other peaks in the synchrotron spectra derive from Ba*L*α and REE*L*α lines, Pb lines from the lead-glass capillary, and Sr, Ba, and LREE escape peaks. Data for Na and Ca cannot be obtained due to the prominent absorption by the surrounding quartz matrix (cf. Fig. 2).

The main interest in the synchrotron-XRF spectra lies therefore in the analysis of the entire REE group with respect to redox-sensitive anomalies, the general shape and slope of the REE pattern, and the determination of other trace elements. Two methods were employed to evaluate the spectra with respect to the REE: (1) normalization of REE peak area determinations against La and C1 chondrite, yielding qualitative (peak area element/peak area La)/(C1/La) REE patterns (Fig. 6a); and (2) a quantification of the spectra to obtain sample/C1 patterns (Figs. 6b and 6c). The first method was applied because it uses primary spectral data and is independent of the quantification procedure. The consistency between the REE pattern obtained by the two methods demonstrates that the method of quantification yields reliable results. The Eu anomaly is apparent in both patterns. The reason for the slightly steeper slope of the normalized pattern in Figure 6a is that, in contrast to the quantified spectra, the variation of the fluorescence cross sections within the group of REEs is neglected here.

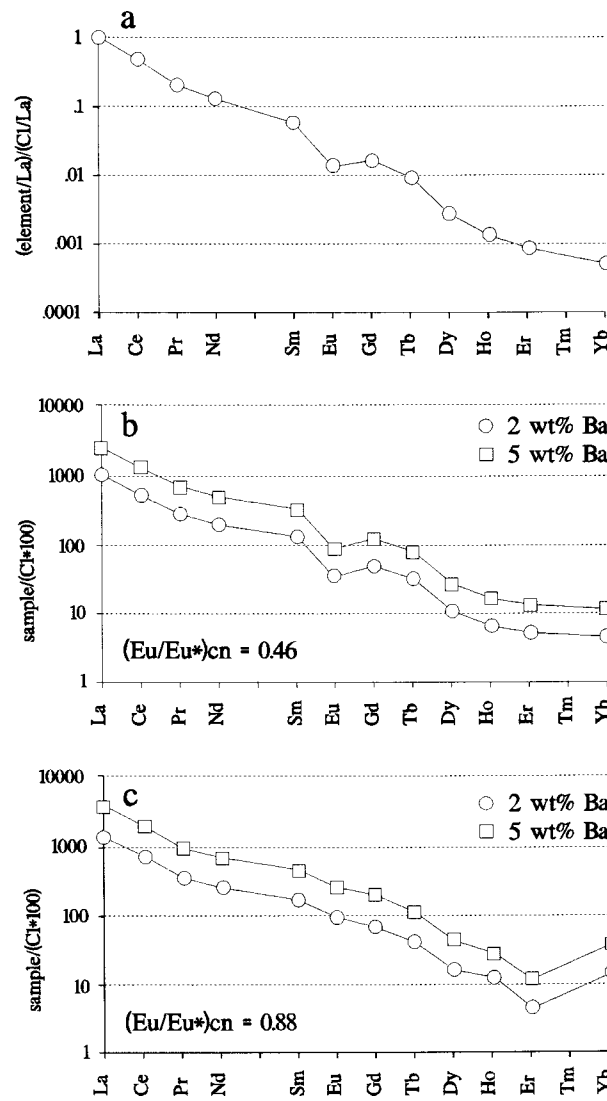

FIGURE 6. Synchrotron-XRF data for La and the other REE in the burbankite crystals. **(a)** Normalization of peak area determinations for REE against La and against C1, analysis bb4975; see text for further explanations. **(b)** Quantified REE pattern of the burbankite in **(a)** for 2 and 5 wt% BaO, respectively, analysis bb4975. **(c)** Quantified REE pattern of a burbankite crystal, analysis bb5381. Data from Table 2.

For the purpose of quantification, Ba was chosen as an internal reference element because it is the element showing the least fluctuation in all measured burbankite crystals. Barium displays a relatively narrow compositional range of 2–5 wt% Ba for all EDX analyses performed (Table 1). Moreover, Ba is a close neighbor of the REE group of elements with respect to atomic weight. As with the REE, the *K* lines are therefore affected very little by absorption (Fig. 2). Two burbankite crystal SXRF analyses are depicted in Table 2, quantified for 2 and 5 wt% Ba, respectively. The quantification of the synchrotron-

XRF spectra yields the same compositional range as the EDX data, e.g., La being between 2.0 and 6.5 wt% (compare Table 1). On a chondrite-normalized basis, a comparison between EDX-derived (Fig. 5) and SXRF-derived (Fig. 6) REE patterns shows that La is slightly above 1–3 × 10^5 times the chondritic value for both methods. Moreover, the slope between La and Nd of nearly one order of magnitude is the same for both methods. This argument is evidence that the quantification procedures for both the EDX and the SXRF spectra yield reliable results.

The REE patterns display a decrease of between 2 and 3 orders of magnitude from La to Yb, reflecting the steep REE fractionation and LREE enrichment typical of carbonatite rocks. The two burbankite analyses (Figs. 6a and 6b) differ only with respect to Eu, which displays a negative anomaly [$(Eu/Eu^*)_{cn}$ = 0.46] in spectrum bb4975 and a rather smooth pattern [$(Eu/Eu^*)_{cn}$ = 0.88] in bb5381. A compilation of all burbankite spectra shows that $(Eu/Eu^*)_{cn}$ = 0.5–1.0 (Fig. 7). Any intermediate value of the Eu anomaly can be observed. Accordingly, a small negative Eu anomaly may be developed in the burbankite crystals.

Some spectra display a relative increase at Yb (e.g., analysis bb5381; Fig. 6c), which is taken to represent an overestimation of absolute values and not an anomaly. It can be observed that, the lower the count rates, the more positive are the chrondrite-normalized anomalies developed in odd atomic numbers, firstly with Tm, then with Ho, and ultimately also with Tb. At the same time, the entire HREE level increases so that the elements with even atomic numbers (e.g., Yb, Er) are also affected. The reason for these anomalies and generally decreasing $(La/Yb)_{cn}$ with decreasing count rates seems to be that the peak areas are overestimated when the detection limits are approached. Therefore, Tm is not given in the patterns but can be interpolated assuming a straight HREE pattern as seen for all other REE.

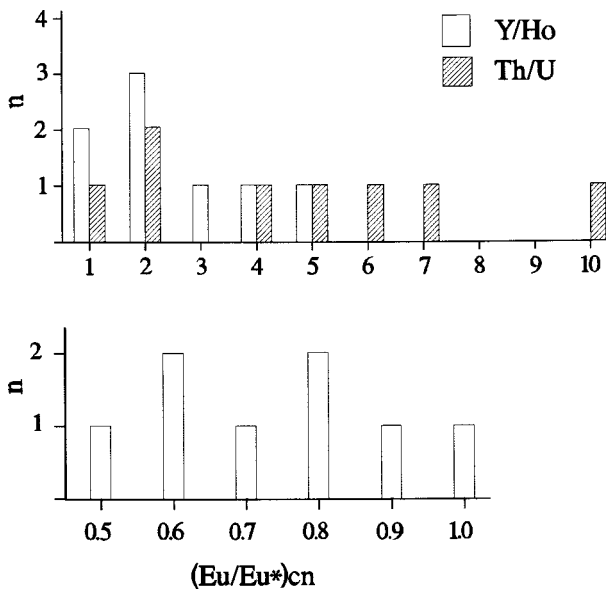

FIGURE 7. Plot of Th/U, Y/Ho, and the Eu anomaly for eight burbankite crystals in fluid inclusions.

TABLE 2. Quantification of synchrotron-XRF spectra

Sample	bb4975	bb4975	bb5381	bb5381
Y (ppm)	93	234	90	229
Ba*	20000	50000	20000	50000
La	23070	57690	24870	62190
Ce	32690	81750	35460	88670
Pr	2360	5900	2529	6321
Nd	8916	22280	9323	23290
Sm	1859	4648	1997	4993
Eu	199	496	447	1116
Gd	942	2353	1190	2972
Tb	115	286	116	290
Dy	256	638	326	813
Ho	36	91	44	115
Er	78	195	28	60
Yb	72	180	188	468
Th	208	528	306	776
U	35	89	61	155
Th/U	5.9	5.9	5.0	5.0
Y/Ho	2.6	2.6	2.0	2.0
(Eu/Eu*)cn	0.46	0.46	0.88	0.88

* Calibration on 2 and 5 wt% Ba, respectively.

The concentrations of Th and U can be determined reliably from the synchrotron-XRF spectra. For the two burbankite analyses presented here, Th concentrations are 208 and 528 ppm for bb4975 (at 2 and 5 wt% Ba, respectively), and 306 and 776 ppm Th for bb5381. The U values are between 35 and 89 ppm U for bb4975, and between 61 and 155 ppm U for bb5381 (both at 2 and 5 wt% Ba, respectively, Table 2). The Th/U ratio therefore can be calculated at 5.9 for bb4975 and 5.0 for bb5381. For eight analyzed burbankite grains, Th/U ranges between 1 and 10 (Fig. 7). These ratios do not differ greatly from the chondritic value of 3.6 (Anders and Grevesse 1989).

The Y/Ho ratios in burbankite crystals range from 1 to 5 (Fig. 7). The two analyses presented in Table 2 yield 2.6 and 2.0, respectively. In contrast to Th$L\alpha$, U$L\alpha$, and Ho$K\alpha$, Y$K\alpha$ will experience minor absorption in the quartz matrix (Fig. 2). A correction for 5% absorption of Y at 30 μm inclusion depth relative to the poorly absorbed Ho, would increase the Y/Ho ratio only in the first decimal place. The Y/Ho ratios therefore are far below the chondritic value of 28 (Anders and Grevesse 1989).

DISCUSSION AND CONCLUSIONS

A comparison of our data with published burbankite analyses is given in Table 1. These data include the first recognized occurrence of burbankite in an alkaline rock (shonkinite) by Pecora and Kerr (1953), later reanalyzed by Effenberger et al. (1985), burbankite from the Bearpaw Mountains (Pecora and Kerr 1953), the occurrence in the Khibina carbonatites (Zaitsev et al. 1998), and burbankite from the lacustrine sediments of the Green River Formation, Wyoming (Fitzpatrick and Pabst 1977). The chemical compositions of burbankite vary widely with respect to all constituents, an observation also made by Zaitsev et al. (1998). This holds not only for burbankite from different localities, but even for burbankite within a single

carbonatite complex and also for the crystals in fluid inclusions studied here. The Na/Ca ratio varies appreciably in rock-forming burbankite and in the crystals detected in the fluid inclusions. The spread in Na/Ca ratios of the burbankite crystals studied is believed to be due to extremely inhomogeneous conditions of fluid entrapment and/or necking-down features. As is evident from optical examination, each fluid inclusion must be regarded as a specific entity with an individual fluid composition. The Na/Ca ratio of burbankite, therefore, depends on the individual fluid composition and on the associated mineral assemblage. The burbankite crystals display overall higher Na/Ca ratios than the literature data although, as previously noted, absorption effects for light elements would lower these ratios even further. The generally high Na/Ca ratios show that a pristine portion of an alkali-rich carbonatitic fluid has been trapped.

The REE concentrations and the chondrite-normalized REE patterns of the burbankite crystals are similar to those of the Khibina carbonatites and the Montana sample (Table 1). The synchrotron-XRF data reported here possibly provide the only complete REE data for burbankite currently available, so that a comparison with published REE patterns can only relate to the LREE. As a result, no Eu analyses have been reported in the literature. The present data show the existence of small negative Eu anomaly in burbankite, which is taken to represent the nature of the carbonatite-derived fluid. An extremely Sr-rich burbankite with 32.4 wt% SrO was reported by Chen and Chao (1974) from alkaline rocks of Mont St. Hilaire in Canada, but this data set does not include the REE. Vanvelthuizen et al. (1995) described a Ca-rich variety of burbankite (calcioburbankite) also from the alkaline complex at Mont St. Hilaire, which has much higher ΣREE but less Sr and Ba than any of the other burbankite specimens listed in Table 1.

The low totals of some of the EDX analyses are noteworthy (Nos. 45 and 70, Table 1). These totals might reflect the presence of an unanalyzed component in appreciable quantities. Fitzpatrick and Pabst (1977) also observed low totals—some below 90 wt% in their samples from the Green River Formation (Table 1)—and suggested that this is due to the presence of submicroscopic organic "kerogen." The Raman spectra, however, do not provide support for an additional organic component in the burbankite crystals studied here. Therefore, the low totals most likely are related to uncertainties in the quantification of the spectra, as outlined in a previous section.

The mere presence of REE,Sr,Ba-carbonates as an abundant solid in carbonatite-derived fluids shows the capability of such H_2O-CO_2-F-Cl fluids to dissolve and transport HFS and LIL elements in the percent range. Their entrapment in fluid inclusions in the quartzite country rock of the Kalkfeld carbonatite, from which they derive, suggests that such highly element-loaded but low-viscosity carbonatite melts/fluids are able to circulate and penetrate country rocks as easily as low-density aqueous or carbonic fluids. "Carbothermal" fluid processes operating in this environment (Rankin et al. 1993), therefore, have the potential to produce economic deposits of REE, Ba, and Sr without requiring large-scale convective fluid systems and high water-rock ratios typically envisaged for other magmatic-hydrothermal ore-forming environments (e.g., Hedenquist and Lowenstein 1994).

ACKNOWLEDGMENTS

This study was largely conducted during a sabbatical leave of BB to Kingston University. We thank the European Union for sponsoring the visit through the Marie Curie Program (TMR) granted to BB and AHR. We thank LabRam Analytical Raman Systems and Renishaw Plc. for generous access to their Laser Raman facilities. Many thanks go to Bill Edwards for advice and help with the SEM-EDX facilities at Kingston, and to Lazlo Vincze, University of Antwerp (Belgium), for providing the computer code for quantitative synchrotron-XRF analysis. Frances Wall (Natural History Museum, London, U.K.) kindly provided a burbankite reference specimen. We further acknowledge access to the Synchrotron-XRF facilities made possible through the Hamburg Synchrotron Laboratory, Germany. Additional financial support was provided by the Deutsche Forschungsgemeinschaft (Bu-826/3-1,2). We thank R.F. Dymek, E. Essene, J.M. Hanchar, D. London, R.J. Bodnar, and S.R. Sutton for comments and useful suggestions made on an earlier version of the manuscript.

REFERENCES CITED

Anders, E. and Grevesse, N. (1989) Abundances of the elements: Meteoritic and solar. Geochimica et Cosmochimica Acta, 53, 197–214.

Anthony, E.Y., Reynolds, T.J., and Beane, R.E. (1984) Identification of daughter minerals in fluid inclusions using scanning electron microscopy and energy-dispersive analysis. American Mineralogist, 69, 1053–1057.

Burt, D.M. (1989) Compositional and phase relations among rare earth element minerals. In Mineralogical Society of America Reviews in Mineralogy, 21, 259–307.

Chen, T.T. and Chao, G.Y. (1974) Burbankite from Mont St. Hilaire, Quebec. Canadian Mineralogist, 12, 342–345.

Effenberger, H., Kluger, F., Paulus, H., and Wölfel, E.R. (1985) Crystal structure refinement of burbankite. Neues Jahrbuch für Mineralogie Monatshefte, 4, 161–170.

Farrow, C.E.G., Watkinson, D.H., and Jones, P.C. (1991) Fluid inclusions in sulfides from North and South Range Cu–Ni–PGE deposits, Sudbury structure, Ontario. Economic Geology, 89, 647–655.

Fitzpatrick, J. and Pabst, A. (1977) Burbankite from the Green River Formation, Wyoming. American Mineralogist, 62, 158–163.

Haller, M. and Knöchel, A. (1996) X-ray fluorescence analysis using synchrotron radiation (SYXRF). Journal of Trace and Microprobe Techniques, 14, 461.

Harris, D.C. (1972) Carbocernaite, a Canadian occurrence. Canadian Mineralogist, 11, 812–813.

Hedenquist, J.W. and Lowenstein, J.B. (1994) The role of magmas in the formation of hydrothermal ore deposits. Nature, 370, 519–527.

Janssens, K., Vincze, L., Vekemans, B., Adams, F., Haller, M., and Knöchel, A. (1998) Use of lead-glass capillaries for micro-focusing of highly-energetic (0-60 keV) synchrotron radiation. Journal of Analytical Atomic Spectrometry, 13, 339–350.

Mavrogenes, J.A., Bodnar, R.J., Anderson, A.J., Bajt, S., Sutton, S.R., and Rivers, M.L. (1995) Assessment of the uncertainties and limitations of quantitative elemental analysis of individual fluid inclusions using synchrotron X-ray fluorescence (SXRF). Geochimica et Cosmochimica Acta, 59, 3987–3995.

Metzger, F.W., Kelly, W.C., Nesbitt, B.E., and Essene, E.J. (1977) Scanning electron microscopy of daughter minerals in fluid inclusions. Economic Geology, 72, 141–152.

Milton, C. and Fahey, J.J. (1960) Classification and association of the carbonate minerals of the Green River Formation. American Journal of Science, 258-A, 242–246.

Miyawaki, R. and Nakai, I. (1996) Crystal chemical aspects of rare earth minerals. In A.P. Jones, F. Wall, and C.T. Williams, Eds., Rare Earth Minerals: Chemistry, origin and ore deposits, p. 21–40. Chapman and Hall, London.

Molnar, F., Watkinson, D.H., Jones, P.C., and Gatter, I. (1997) Fluid inclusion evidence for hydrothermal enrichment of magmatic ore at the contact zone of the Ni-Cu-Platinum-Group-Element 4b deposit, Lindsley Mine, Sudbury, Canada. Economic Geology, 92, 674–685.

Pecora, W.T. and Kerr, J.H. (1953) Burbankite and calkinsite, two new carbonate minerals from Montana. American Mineralogist, 38, 1169–1183.

Philippot, P., Menez, B., Chevalier, P., Gibert, F., Legrand, F., and Populus, P. (1998) Absorption correction procedures for quantitative analysis of fluid inclusions using synchrotron radiation X-ray fluorescence. Chemical Geology, 144, 121–136.

Prins, P. (1981) The geochemical evolution of the alkaline and carbonatite complexes of the Damaraland igneous province, South West Africa. Annales Universiteit Stellenbosch, 3, Serie A1, 145–278.

Rankin, A.H. and Le Bas, M.J. (1974) Nahcolite ($NaHCO_3$) in inclusions in apatites from some E. African ijolites and carbonatites. Mineralogical Magazine, 39, 564–570.

Rankin, A.H., Wilkinson, J.J., Nolan, J., and Croudace, I. (1993) Carbothermal fluids and gold mineralization: where are the gold-bearing carbonatites? Terra Nova, 5, 439–440.

Roedder, E. (1990) Fluid inclusions analysis—prologue and epilogue. Geochimica

et Cosmochimica Acta, 54, 495–507.
Speer, J.A. (1990) Crystal chemistry and phase relations of orthorhombic carbonates. In Mineralogical Society of America Reviews in Mineralogy, 11, 145–190.
Ting, W., Burke, E.A.J., Rankin, A.H., and Woolley, A.R. (1994) Origin and significance of CO_2, H_2O and CH_4 fluid inclusions in apatite from the Sukulu carbonatite complex, Uganda. European Journal of Mineralogy, 6, 787–803.
Vanko, D.A., Sutton, S.R., Rivers, M.L., and Bodnar, R.J. (1993) Major-element ratios in synthetic fluid inclusions by synchrotron X-ray fluorescence microprobe. Chemical Geology, 109, 125–134.
Vanvelthuizen, J., Gault, R.A., and Grice, J.D. (1995) Calcioburbankite, $Na_3(Ca,REE,Sr)_3(CO_3)_5$, a new mineral species from Mont Saint Hilaire, Quebec, and its relationship to the burbankite group of minerals. Canadian Mineralogist, 33, 1231–1235.
Verwoerd, W.J. (1963) Rare-earth minerals from South African carbonatites. Annals Geological Survey South Africa, 2, 119–135.
Vincze, L. (1995) Monte Carlo simulation of conventional and synchrotron XRF spectrometers. Ph.D. dissertation, University of Antwerp, Belgium.
Wall, F., Le Bas, M.J., and Srivastava, R.K. (1993) Calcite and carbocernaite exsolution and cotectic textures in a Sr,REE-rich carbonatite dyke from Rajasthan, India. Mineralogical Magazine, 57, 495–513.
Wolff, J.A. (1994) Physical properties of carbonatite magmas inferred from molten salt data, and application to extraction patterns from carbonatite-silicate magma chambers. Geological Magazine, 131, 145–153.
Xie Yihan, Fan Hargrui, and Wang Ying Ian (1996) REE daughter minerals in fluid inclusions in the giant Bayan Obo REE-Fe-Nb ore deposit: discovery and implications. Asian and Pacific International Fluid Inclusion Society, Newsletter 1, 26–27.
Zaitsev, A.N., Wall, F., and Le Bas, M.J. (1998) REE-Sr-Ba minerals from the Khibina carbonatites, Kola Peninsula, Russia: their mineralogy, paragenesis and evolution. Mineralogical Magazine, 62, 225–250.

MANUSCRIPT RECEIVED JUNE 30, 1998
MANUSCRIPT ACCEPTED JANUARY 12, 1999
PAPER HANDLED BY DAVID LONDON